Dynamic Adjustment of the Ocean Circulation to Self-Attraction and Loading Effects

Citation: Vinogradova, Nadya T., Rui M. Ponte, Katherine J. Quinn, Mark E. Tamisiea, Jean-Michel Campin, and James L. Davis. "Dynamic Adjustment of the Ocean Circulation to Self-Attraction and Loading Effects." Journal of Physical Oceanography 45, no. 3 (March 2015): 678–689. © 2015 American Meteorological Society

As Published: http://dx.doi.org/10.1175/jpo-d-14-0150.1

Publisher: American Meteorological Society

Persistent URL: http://hdl.handle.net/1721.1/98389

Version: Final published version: final published article, as it appeared in a journal, conference proceedings, or other formally published context

Dynamic Adjustment of the Ocean Circulation to Self-Attraction and Loading Effects

NADYA T. VINOGRADOVA, RUI M. PONTE, AND KATHERINE J. QUINN

Atmospheric and Environmental Research, Lexington, Massachusetts

MARK E. TAMISIEA

National Oceanography Centre, Liverpool, United Kingdom

JEAN-MICHEL CAMPIN

Massachusetts Institute of Technology, Cambridge, Massachusetts

JAMES L. DAVIS

Lamont-Doherty Earth Observatory, Columbia University, Palisades, New York

(Manuscript received 23 July 2014, in final form 2 December 2014)

ABSTRACT

The oceanic response to surface loading, such as that related to atmospheric pressure, freshwater exchange, and changes in the gravity field, is essential to our understanding of sea level variability. In particular, so-called self-attraction and loading (SAL) effects caused by the redistribution of mass within the land–atmosphere–ocean system can have a measurable impact on sea level. In this study, the nature of SAL-induced variability in sea level is examined in terms of its equilibrium (static) and nonequilibrium (dynamic) components, using a general circulation model that implicitly includes the physics of SAL. The additional SAL forcing is derived by decomposing ocean mass anomalies into spherical harmonics and then applying Love numbers to infer associated crustal displacements and gravitational shifts. This implementation of SAL physics incurs only a relatively small computational cost. Effects of SAL on sea level amount to about 10% of the applied surface loading on average but depend strongly on location. The dynamic component exhibits large-scale basinwide patterns, with considerable contributions from subweekly time scales. Departures from equilibrium decrease toward longer time scales but are not totally negligible in many places. Ocean modeling studies should benefit from using a dynamical implementation of SAL as used here.

1. Introduction

The concern over rising sea level has led to numerous modeling studies and assessments of observational evidence from satellite altimetry, tide gauges, and other related datasets [see, e.g., Stocker et al. (2014), Church et al. (2011), and Milne et al. (2009) for a review]. However, because variability in sea level represents an integration of many aspects of climate change, to formulate projections and to understand contemporary changes in sea level involves consideration of changes in the hydrosphere and cryosphere, as well as the solid Earth, and the complexity of the problem remains challenging (e.g., Stammer et al. 2013). Ocean dynamics and associated redistributions of heat and freshwater are one of the major contributors to variability in sea level on a variety of time and spatial scales (Landerer et al. 2007; Yin et al. 2010; Stammer et al. 2013). Changes in ocean circulation can also affect the distribution of mass over the globe. The variable oceanic mass field in turn loads Earth and changes its gravity field through the processes of self-gravitation and crustal deformation. The ocean responds to such gravity field perturbations by adjusting its mass (and sea level) fields. Such adjustments are commonly referred to as self-attraction and loading (SAL) effects and can have a measurable impact on sea level (Mitrovica et al. 2001; Tamisiea et al. 2010). Their importance for tidal studies

Corresponding author address: Nadya Vinogradova, Atmospheric and Environmental Research, 131 Hartwell Ave., Lexington, MA 02421.
E-mail: nadya@aer.com

DOI: 10.1175/JPO-D-14-0150.1

has long been recognized, as discussed by Ray (1998) and Arbic et al. (2004).

The theory of SAL, which describes the effects of self-gravitation and associated changes in geopotential and deformation of the ocean floor, has been formulated in the early works of Farrell and Clark (1976) and applied, for example, to tide gauge records to estimate implied twentieth-century land ice melting rates (Mitrovica et al. 2001) and understand the seasonal cycle in sea level (Tamisiea et al. 2010). Other studies have focused on the impact of SAL effects on variations in ocean mass on monthly to decadal time scales using GRACE (Vinogradova et al. 2011; Riva et al. 2010) and in situ bottom pressure data (Vinogradova et al. 2010). The effects of SAL on longer time scales, up to centennial, were discussed by Kopp et al. (2010). In all those studies, SAL effects are inferred by solving a sea level equation under the assumption that the ocean's response to SAL is static and in equilibrium with the forcing. In such cases, the ocean is assumed to shift mass around rapidly and maintain negligible horizontal pressure gradients. While the equilibrium assumption is expected to hold at sufficiently low frequencies, the exact dependence on time scale was never properly addressed before and is one motivation of the present study.

One way to account for possible nonequilibrium sea level signals is to implement SAL physics in ocean general circulation models, but such instances are rare in part because of the high computational costs that can be involved. Among the first attempts of such implementation are studies by Stepanov and Hughes (2004) and Kuhlmann et al. (2011), who considered SAL within barotropic and baroclinic ocean models, respectively. In particular, Stepanov and Hughes (2004) show that integrating a model with the calculation of SAL effects, using a ''prohibitively expensive'' global convolution integral at each grid point and time step, can ''occupy more than 90%'' of the computing time. Kuhlmann et al. (2011) used a different computational approach based on spherical harmonics decomposition to incorporate SAL physics in their model. Their experiments were more successful in terms of computational efficiency, increasing computing time by only ~16%.

Here, we expand on these studies by implementing the physics of SAL in a baroclinic ocean model and focusing, in particular, on the possibility of having sea level dynamic signals induced by the SAL effects. Such deviations from equilibrium can depend on several factors, including coastal geometry, bottom topography, and so on. Drawing parallels with the ocean response to surface loading related to atmospheric pressure (Ponte 1993) and freshwater fluxes (Ponte 2006), such nonequilibrium signals are expected to be more significant for short time scales and in shallow and enclosed coastal regions.

In this initial SAL study, the only mass variations producing SAL effects are those induced by the ocean circulation. For simplicity, effects from other mass loadings such as those associated with land water, ice, and atmospheric pressure and discussed, for example, by Tamisiea et al. (2010) and Vinogradova et al. (2010, 2011) are not addressed here. In what follows, we describe the physics of SAL and its implementation in the ocean model in section 2, examine the results focusing on sea level variability induced by the SAL effects in section 3, and discuss the nonequilibrium response as a function of time scale and location in section 4. Summary and conclusions are presented in section 5.

2. Approach

a. Basic equations

Following Farrell and Clark (1976) and Stepanov and Hughes (2004), the vertical displacement of the geoid relative to the seafloor resulting from a unit mass at angular distance α can be written in the form of a Green's function as

$$G(\alpha) = \frac{R_e}{m_e} \sum_{n=0}^{\infty} (1 + k'_n - h'_n) P_n(\cos\alpha), \qquad (1)$$

where P_n are the Legendre polynomials, k'_n and h'_n are the elastic loading Love numbers that can be determined from a number of Earth models, and R_e and m_e are Earth's radius (6.371×10^6 m) and mass (5.9736×10^{24} kg), respectively. The constant of proportionality equal to $(1 + k'_n - h'_n)$ represents the three effects of SAL, namely, the gravitational attraction induced by the point load, the loading effect that accounts for gravitational changes in response to the load (k'_n), and the loading effect describing how Earth will deform under the additional mass (h'_n).

In what follows, we take the thin shell approximation and assume that the location of mass anomalies in the water column does not matter and that the respective SAL effects are not a function of depth, which are reasonable considerations given the large aspect ratio of horizontal and vertical scales in the ocean. Consider then a two-dimensional field $\zeta^b(\theta, \lambda)$, where θ is latitude and λ is longitude, taken to represent mass anomalies vertically integrated over the full ocean depth. For the purposes of this paper, we can treat ζ^b as a field of ocean bottom pressure anomalies in equivalent water thickness units. To estimate the perturbation forcing load ζ^F due to SAL effects, one needs to perform a convolution of the Green's function [Eq. (1)] with ζ^b, that is,

$$\zeta^F(\theta,\lambda) = \rho_0 R_e^2 \iint \zeta^b(\theta',\lambda') G(\alpha) \sin\theta' \, d\theta' \, d\lambda', \quad (2)$$

where ρ_0 is the mean density of seawater, and α is the angular distance between (θ, λ) and (θ', λ'). To implement SAL effects directly in numerical models requires the evaluation of this convolution integral at every time step and over the entire ocean, which is very computationally expensive (Stepanov and Hughes 2004). However, if we decompose ζ^b into spherical harmonics, convolution becomes a multiplication and is much faster. Following Ray (1998), the convolution in spherical harmonics becomes

$$\zeta^F_{nm} = \frac{3\rho_0(1 + k'_n - h'_n)}{\rho_e(2n+1)} \zeta^b_{nm}, \quad (3)$$

where n and m are the degree and order of the spherical harmonic decomposition, and ρ_e is the mean density of Earth [$\rho_e = 3m_e/(4\pi R_e^3) = 5517\,\mathrm{kg\,m^{-3}}$]. The computational cost then becomes mostly associated with transforming between grid space and spherical harmonics, but as discussed below, one can make use of efficient and readily available transform algorithms for significant computational gains.

b. Implementing SAL physics in an ocean model

Similar to atmospheric pressure forcing in a baroclinic ocean (Ponte and Vinogradov 2007), the effects of ζ^F can be applied as an additional surface load or body force. At each model time step, the computed hydrostatic pressure anomaly can be used to derive anomalous mass ζ^b (ocean bottom pressure fields). According to the physics of SAL, the anomalous mass ζ^b gives rise to gravitational potential perturbations defined by ζ^F that are computed using Eq. (3). To calculate the ocean response to these perturbations, the body force resulting from ζ^F is applied as an additional pressure gradient acting at every model layer over the next time step. The process of computing ζ^b, inferring from it the corresponding ζ^F fields, and then applying ζ^F as an additional surface load is performed at every model time step.

The above approach is implemented within the Massachusetts Institute of Technology (MIT) general circulation model [MITgcm; an evolved form of the model described in Marshall et al. (1997), Adcroft et al. (2004), and Campin et al. (2008)], which has an option to include surface loading such as atmospheric pressure in its forcing fields. The model setup used here provides an estimate of the ocean state on a 1° horizontal grid (but refined to about 1/3° near the equator in the meridional direction) and includes a dynamic sea ice component (Losch et al. 2010; Heimbach et al. 2010). Subgrid-scale parameterization of vertical mixing is achieved via the nonlocal K-profile parameterization (KPP) scheme of Large et al. (1994) and parameterization of geostrophic eddies are by Redi (1982) and Gent and McWilliams (1990). The model setup is that created by Gael Forget (MIT) as part of the latest version of the ECCO state estimates discussed in more detail by Wunsch and Heimbach (2013) and Speer and Forget (2013).

To implement SAL physics in the MITgcm, we have created a suite of codes that include Eq. (3), spherical harmonic decomposition, regridding routines, and so on and organized them using the basic MITgcm packaging structure so that one can easily enable and disable SAL physics if needed. The package is computationally efficient, and for the experiments considered here the inclusion of SAL physics leads to an increase of the computation time by less than 6% (timing tests were based on runs on 8 and 16 processors). The efficiency is in part because of a fast and accurate method of forward and inverse transform from a spatial grid to spherical harmonics and back. Here, we used the spherical harmonics software package SHTOOLS, developed by M. Wieczorek, which is freely available and includes routines that use the Driscoll and Healy (1994) sampling theorem to transform an equally spaced grid into spherical harmonics and the inverse transform. This sampling theorem, together with the use of a fast Fourier transform algorithm in longitude, requires $O(N^2 \log N^2)$ operations to transform a $N \times N$ grid, versus $O(N^4)$ operations using the basic formulas (Blais and Provins 2002). For our purposes, N was set to 360, which was chosen as a trade-off between computational cost and minimization of interpolation errors and which defines the maximum degree in spherical harmonic decomposition $l = N/2 - 1 = 179$. The spherical harmonic truncation to degree 179 is equivalent to 1° horizontal grid resolution. We use this maximum truncation degree because it is consistent with the ocean model resolution. Also, the computation of SAL is an inherent smoother that tends to minimize interpolation and truncation errors. The timing test for transforming the 1° grid to spherical harmonics and the inverse transform back to a grid takes ~0.01 s.

c. Experiment design

To compute the sea level response to ζ^F and to isolate it from other sea level signals, we perform a twin experiment where we turn ζ^F on and off, while keeping the other surface forcing the same for both runs. The common atmospheric forcing includes wind and other variables from the European Centre for Medium-Range Weather Forecasts Interim Reanalysis (ERA-Interim)

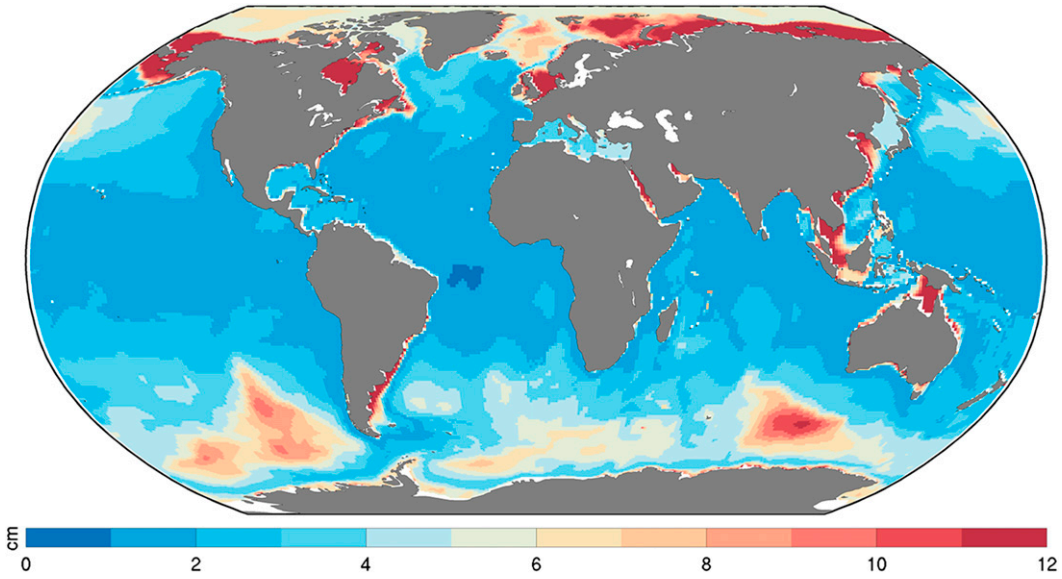

FIG. 1. Standard deviation of ocean mass anomalies ζ^b driven by atmospheric forcing, without forcing due to SAL effects ζ^F. Variability is computed based on 6-hourly output from the MITgcm over a 10-yr integration period (1992–2001). Units are equivalent cm of water thickness.

(Dee et al. 2011). Both runs of the twin experiment are produced by integrating the MITgcm over a 10-yr period from the beginning of 1992 to the end of 2001. The difference between the two model outputs provides an estimate of SAL effects on the ocean. We will denote the difference in sea level outputs as ξ_{SAL}, which represents the changes in sea level due to ζ^F. Model solutions here are produced without any constraints from observations. The choice is deliberate and ensures that no SAL effects are indirectly included in model solutions through data assimilation.

To examine the ocean response to SAL effects on a wide range of time scales, ζ^F is applied as a high-frequency forcing. We began with the time step $\Delta t = 1$ h, integrating the MITgcm for a decade using a backward in time free-surface time-stepping scheme and creating model diagnostics as 6-h-averaged fields. Such output provides a view of the ocean response from periods of 12 h to 10 yr and form the basis of our analysis, unless noted otherwise. To examine the ocean response at very high frequencies (subdaily), we repeat our experiment with a time step $\Delta t = 5$ min, integrating the MITgcm for a few months using the free-surface Crank–Nicholson time-stepping scheme (Campin et al. 2004) and creating model diagnostics as hourly fields. The change of temporal discretization to the Crank–Nicholson time-stepping scheme and the smaller time step were necessary in order to capture high-frequency components that are otherwise damped by the backward in time implicit free-surface scheme, especially with long time step. The reduction of the time step Δt from 1 h to 5 min is necessary to avoid spurious oscillations of the solution when the Crank–Nicholson scheme is used. For both cases of temporal discretization, ζ^F is applied after 5 days of integration to avoid the largest initial transients while the ocean is spun up from a state of rest.

3. SAL effects associated with the variable ocean circulation

To better understand SAL-induced changes in sea level, let us first examine the magnitude of the expected mass variations, in our case those related to the ocean circulation. For most of the oceans, the standard deviation in ζ^b calculated over the 10-yr integration period is relatively small and typically does not exceed a few centimeters of equivalent water thickness (Fig. 1). Noticeable exceptions are shallow coastal regions, parts of the Southern Ocean and Arctic Ocean, where ζ^b standard deviations can reach more than 10 cm. Spatial patterns and amplitudes in Fig. 1 have been discussed in detail in other studies and are in general agreement with previous estimates of ζ^b variability (e.g., Ponte 1999; Vinogradova et al. 2007, 2010, 2011; Quinn and Ponte 2012). We take the variability in Fig. 1 as a good qualitative representation of expected ζ^b signals in the ocean on which to base our exploration of SAL effects in the rest of the paper.

Figure 2 shows the standard deviation of SAL forcing ζ^F corresponding essentially to the mass fluctuations in Fig. 1 and calculated from the run with the SAL physics turned on. As described by Eq. (3), ζ^F tends to be proportional to local mass anomalies. Thus, we expect to

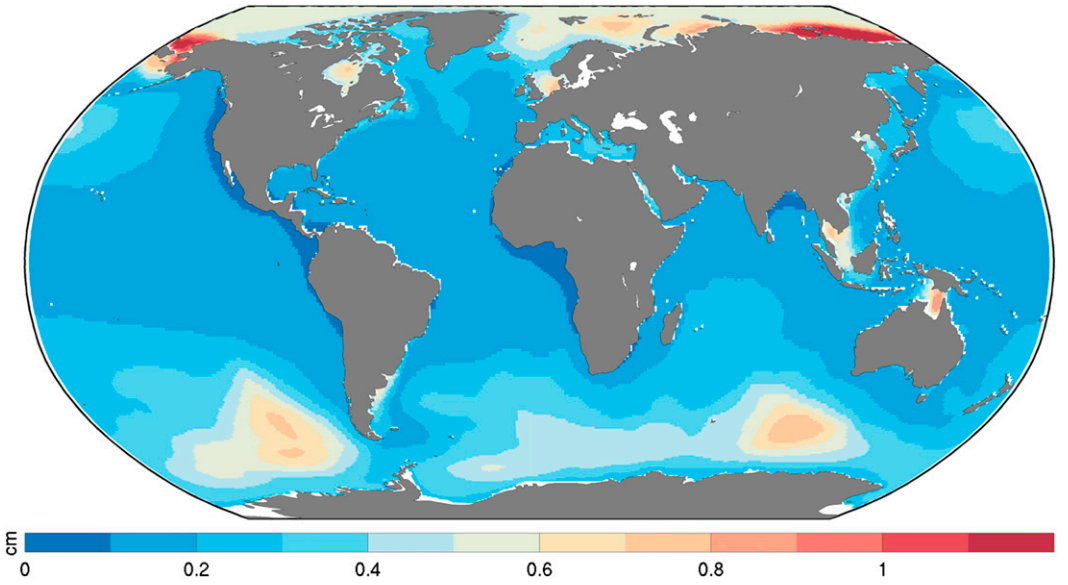

FIG. 2. Standard deviation of forcing ζ^F derived according to Eq. (3).

see stronger variability in ζ^F around the regions with large variations in ζ^b, such as the Southern Ocean, shallow coastal regions of the Indonesian Seas, including the Gulf of Carpentaria, Arctic coast, Hudson Bay, and off the coast of Argentina, where values from 0.5 to 1.5 cm can be attained (Fig. 2). Typical values over most of the deep ocean are only a few millimeters.

One of the common approaches to account for SAL effects is to use a simple parameterization by multiplying the mass field by a constant factor, a practice adopted for tidal models since Accad and Pekeris (1978) (see discussion in Ray 1998). To show possible limitations of such an approximation, Fig. 3 displays the ratio of standard deviations in SAL forcing ζ^F and mass variations ζ^b. On average, variability in ζ^F is about 10% of that in ζ^b, but the ratio exhibits large spatial variations and ranges from 1% to 20%. This implies, in particular, that a simple constant parameterization of SAL effects might not be sufficient, and the need for a full representation of SAL effects is warranted.

The standard deviation of ξ_{SAL}, that is, sea level associated with SAL effects as defined in section 2, shows

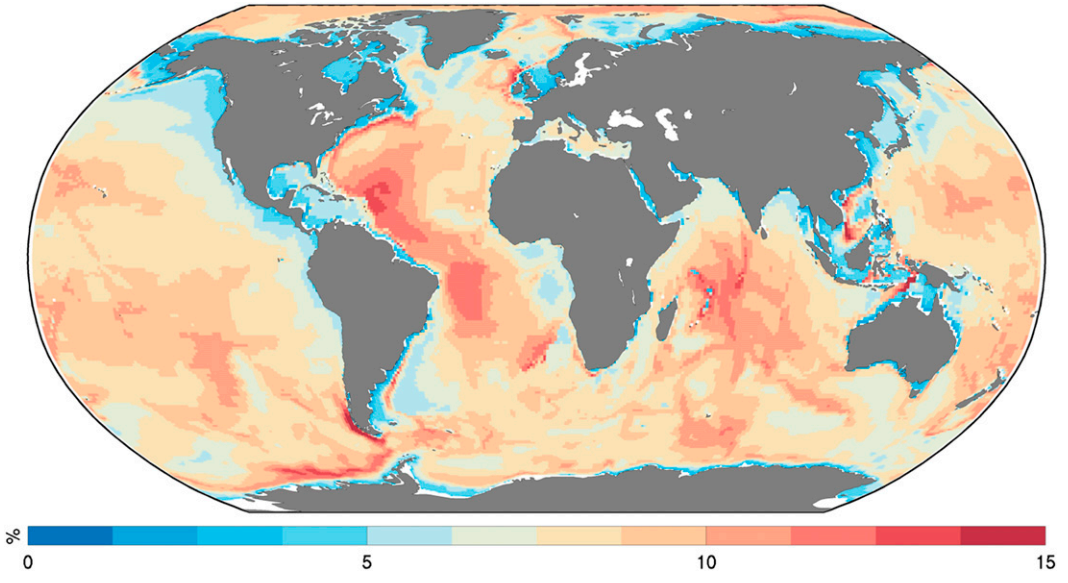

FIG. 3. Percentage ratio of the standard deviation of ζ^F to the standard deviation of ζ^b, using respective values from Figs. 1 and 2.

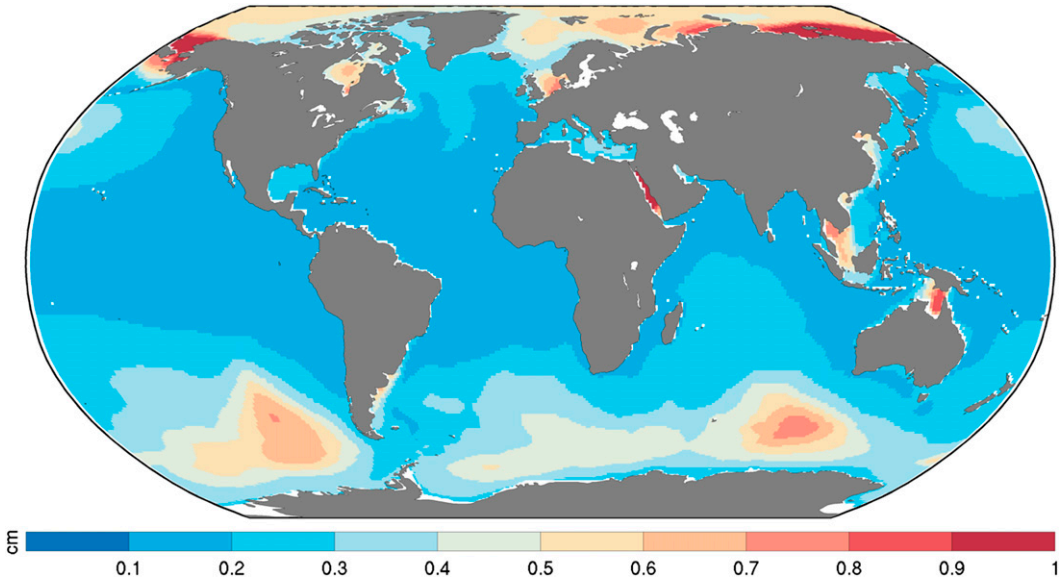

FIG. 4. Standard deviation of SAL-induced sea level ξ_{SAL} for the 10-yr period of study. To isolate the effect of SAL on sea level from other forcing (winds, heat fluxes, etc.), all other signals in sea level have been removed as described in the text.

significant geographical variations (Fig. 4), closely following variability in ζ^F discussed in Fig. 2. Enhanced ξ_{SAL} signals typically coincide with regions of the strongest forcing ζ^F (and ζ^b), with the largest impact found in the Arctic Ocean (East Siberian, Laptev, Kara, and Chukchi Seas), where standard deviations >1 cm are possible; enhanced values in the range of 0.5–1 cm are found in other coastal regions such as the Gulf of Carpentaria, Gulf of Thailand, Hudson Bay, and off the coast of Argentina as well as in the Southern Ocean (Kergulen Plateau and Bellingshausen basin). Given that most ocean models do not include SAL effects in their formulation, Fig. 4 can be treated as an additional model error associated with the missing physics, which is about 0.4 cm on average and can exceed 1 cm in aforementioned regions.

4. Dynamic and equilibrium response

A good way to assess the importance of the dynamic implementation of SAL effects is to examine the relevance of the dynamic response in terms of the departures of sea level from the equilibrium solution. The separation into equilibrium and nonequilibrium (dynamic) components is similar to the analysis of sea level variations related to fluctuations in atmospheric surface pressure, in which the signal is separated into an inverted barometer (IB) response and deviations from it (Ponte 1993, 2006). Following Ponte (1993), the equilibrium response to SAL effects is computed as

$$\xi_{EQ} = \zeta^F - \overline{\zeta^F}, \tag{4}$$

where $\overline{\zeta^F}$ is the spatial average of the forcing over the global ocean. In general, $\overline{\zeta^F}$ is a nonzero term and a function of time. In our case, $\overline{\zeta^F}$ is zero by design, as we remove the spatial mean from the fields used to calculate ζ^F.[1] As a crude test of our procedures, we compared monthly averaged values of ξ_{EQ} with those computed using the sea level equation as in Tamisiea et al. (2010). The formalism by Tamisiea et al. (2010) follows the classic paper by Farrell and Clark (1976) that uses an iterative procedure to estimate the spatial distribution of the relative sea level resulting from the various mass loads. As previously mentioned, the sea level equation approach uses the assumption that the ocean response to the loads is static (i.e., the applied loading is balanced by the resulting sea level gradients), which should hold at monthly and longer time scales. Comparison of the sea level solution with values of ξ_{EQ} reveals that at monthly (and longer) time scales the two equilibrium estimates were indeed essentially equivalent, with the largest differences not exceeding 1 mm in amplitude. Using Eq. (4), the dynamic component ξ_{DYN} is then defined as

[1] The spatial mean of ζ_b has no dynamical significance in terms of inducing horizontal pressure gradients and contains, in fact, spurious contributions caused by the model's Boussinesq formulation (Ponte 1999).

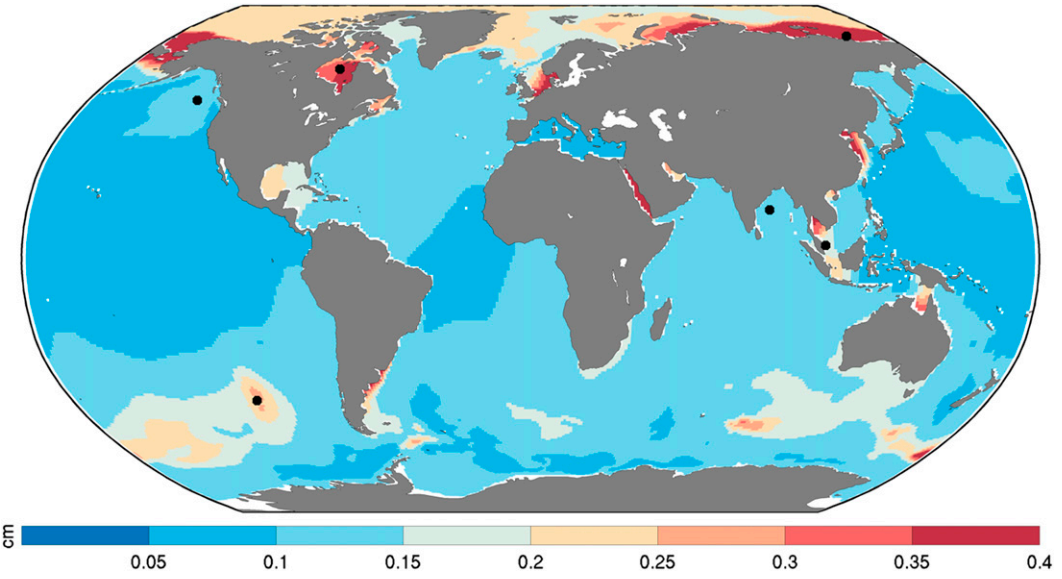

FIG. 5. Standard deviation of the dynamic component of SAL-induced sea level ξ_{DYN}, computed according to Eq. (5). Black dots show the location of time series analyzed in Fig. 7.

$$\xi_{DYN} = \xi_{SAL} - \xi_{EQ}. \quad (5)$$

Pressure gradients associated with ξ_{DYN} and respective currents represent the dynamic response of the ocean to ζ^F.

From the standard deviation of ξ_{DYN} shown in Fig. 5, in most of the open ocean, the departure from equilibrium is typically ~1 mm, but in several coastal regions (e.g., Arctic, Hudson Bay, North Sea, off the coast of Argentina, Gulf of Carpentaria, Gulf of Thailand, and Yellow Sea) ξ_{DYN} standard deviations can reach 3–12 mm. The large-scale patterns in Fig. 5 somewhat resemble those in the forcing in Fig. 2, with larger ξ_{DYN} signals in high latitudes, but there are also visible effects of topography and a general increase of ξ_{DYN} variability over shallow depths and semienclosed regions. As mentioned earlier, SAL effects are traditionally considered to result in a static response; therefore, the values in Fig. 5 can be treated as the errors due to unresolved dynamic behavior under SAL forcing.

For a quantitative assessment of the importance of the dynamic signals, one can look at the ratio of the standard deviation of ξ_{DYN} to that of the forcing ζ^F or equivalently ξ_{EQ}. As Fig. 6a shows, in most of the oceans the ratio is >0.2; values >0.5 are seen in large parts of the Atlantic and Indian Oceans and in several coastal regions can be ~1 or larger. On average, the ratio is ~0.5. These results suggest that the ocean response has a substantial dynamic component over large parts of the domain.

To assess the dependence of the results on time scale, Fig. 6b shows the same ratio but based on time series of ξ_{DYN} and ξ_{EQ} that have been averaged in time over one week. Comparing Figs. 6a and 6b indicates that the strongest dynamic behavior comes from high-frequency, that is, subweekly, oscillations as the ratio in Fig. 6b becomes considerably smaller, about 0.25 on average, apart from a few small regions in the Southern Ocean where ratios are >1.[2] However, despite the general decrease, the ratio in Fig. 6b is still >0.2 in many places, indicating that the departures from equilibrium are not totally negligible at time scales longer than a week and that studies of ξ_{SAL} can benefit from using a dynamical implementation of ζ^F.

To further characterize the tendency for the nonequilibrium response to increase with frequency, ξ_{SAL} and its components are examined in more detail at a few selected locations, which are chosen to represent regions with considerable ξ_{DYN} variability: two open-ocean sites in the South and North Pacific and coastal and near-coastal locations in Hudson Bay, South China Sea, Bay of Bengal, and East Siberian Sea (Fig. 5). At each location we estimate the power spectral density (PSD) by computing a Fourier transform of the autocorrelation functions of ξ_{DYN} and ξ_{EQ}, as well as their ratio

$$r(\omega) = \frac{\mathrm{PSD}(\xi_{DYN})}{\mathrm{PSD}(\xi_{EQ})} \quad (6)$$

[2] The reasons for these substantially higher values remain unclear and may be related to topography or other physical features, but numerical issues are also possible, and thus those results are to be treated with caution.

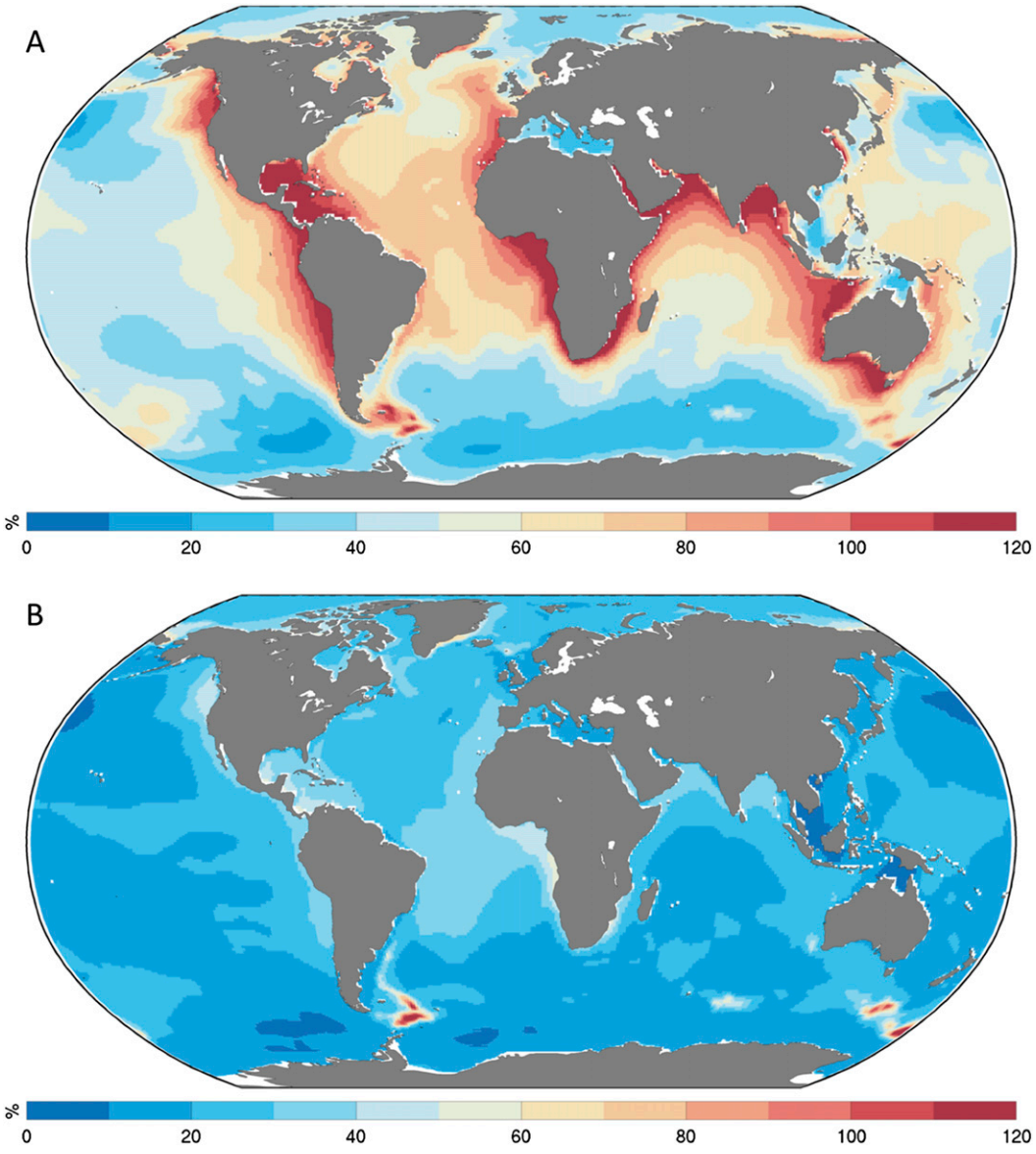

FIG. 6. Ratio of the standard deviation of ξ_{DYN} to the standard deviation of ξ_{EQ} based on (a) 6-hourly fields, that is, using the values from Figs. 5 and 2, and (b) weekly averaged fields of ξ_{DYN} and ξ_{EQ}.

as a function of frequency ω. To best resolve high-frequency fluctuations, the analysis here is done using hourly series of ξ_{DYN} and ξ_{EQ}, which are based on using the Crank–Nicholson time-stepping scheme, as described in section 2c.

Values of $r \sim 1$ indicate that power in ξ_{DYN} and ξ_{EQ} is comparable, ξ_{DYN} is important, and the equilibrium assumption is not valid. Values shown in Fig. 7 (middle panels) suggest that the time scale at which the static approximation becomes a poor estimator of ξ_{SAL} is dependent on the region. For example, in Hudson Bay, $r > 1$ at periods <1 day, but that threshold period can be up to 2 days in the open-ocean regions and up to a week in the East Siberian Sea and Bay of Bengal. In general, the tendency for nonstatic response does increase with frequency. Values of r in Fig. 7 increase by more than a factor of 10 from the longest to the shortest periods. Similar conclusions on the IB approximation were reached by Ponte (1993), who reports global nonequilibrium behavior at periods shorter than ~2 days.

At some locations, for example, Bay of Bengal, the frequency structure of the ξ_{DYN} spectra, including the presence of high-frequency spectral peaks, resembles that of the forcing ξ_{EQ} (see left panels in Fig. 7). Such behavior indicates that the dynamic response is partly locally forced and can result, for example, from an

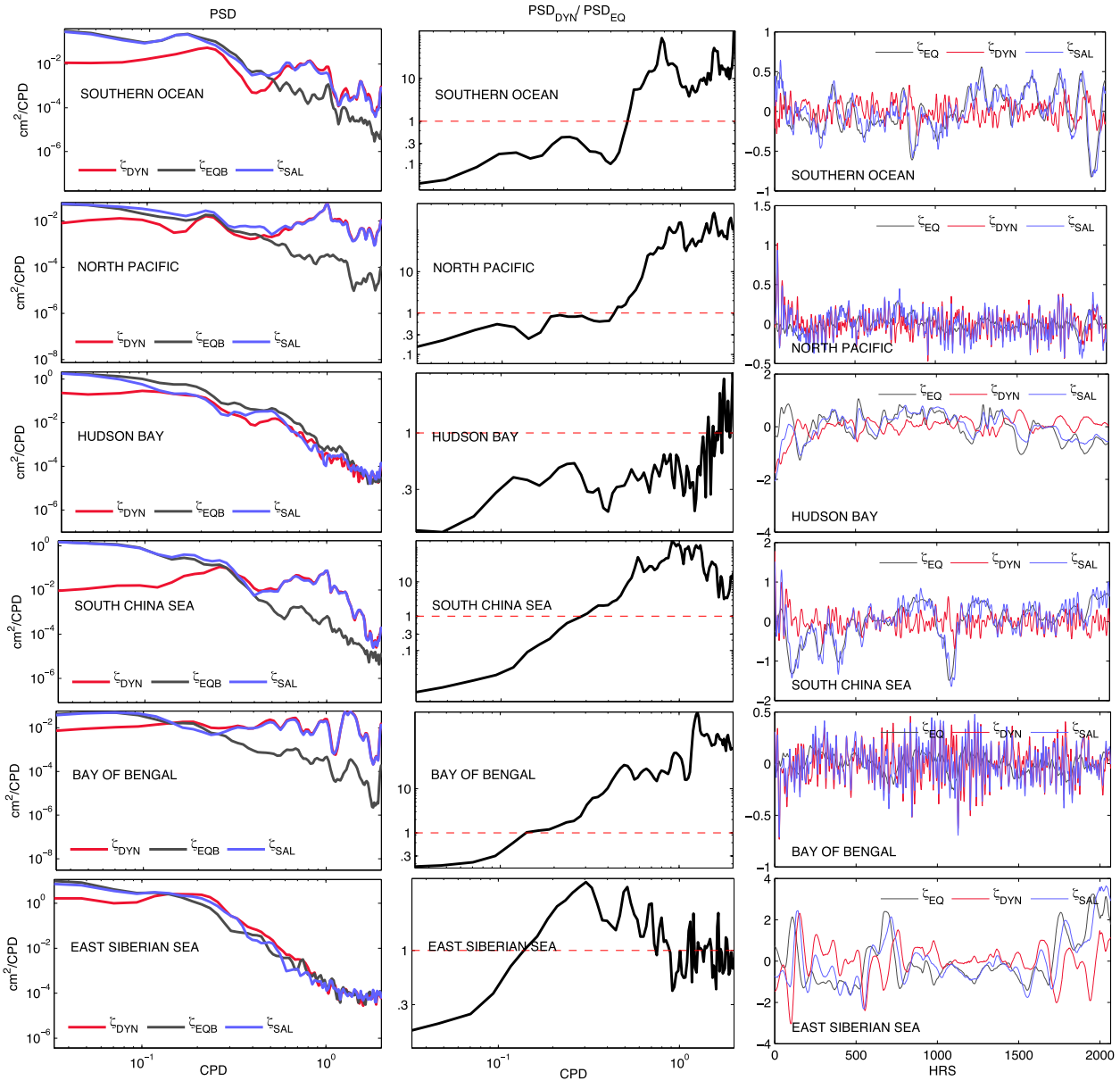

FIG. 7. Power spectra of (left) ξ_{DYN}, ξ_{EQ}, and total ξ_{SAL} and (middle) the ratio of the dynamic to the equilibrium spectral values as a function of frequency computed according to Eq. (6). Spectral estimates use averaging over 20 adjacent frequencies. Abscissa units for left and middle panels are cycles per day, and periods from 12 h to 1 month are shown. (right) Corresponding time series based on hourly data during a 3-month period. Station locations are shown in Fig. 5.

incomplete adjustment to ζ^F. Also suggestive of this is the tendency for ξ_{SAL} to exhibit smaller amplitudes and a slight lag relative to ξ_{EQ} (see, e.g., the Hudson Bay time series in Fig. 7). At other locations, for example, the North Pacific, ξ_{DYN} shows relatively energetic oscillations at nearly daily time scales that are absent in the ξ_{EQ} series. These fluctuations in ξ_{DYN} dominate daily variability in ξ_{SAL}, as seen from the corresponding time series plot, and can be associated with a nonlocal response, such as that of the global mode resonances discussed by Ponte (1993) in the context of the response to atmospheric pressure. Another interesting feature at the North Pacific location is the relatively long time scales at which the dynamic component is relevant. Notice that even at the longest period considered here, that is, ~1 month, the power ratio does not drop below 0.1. Similar behavior is present at other locations as well (e.g., Bay of Bengal and East Siberian Sea).

Besides the expected tendency for nonequilibrium response to occur at sufficiently short time scales, for which

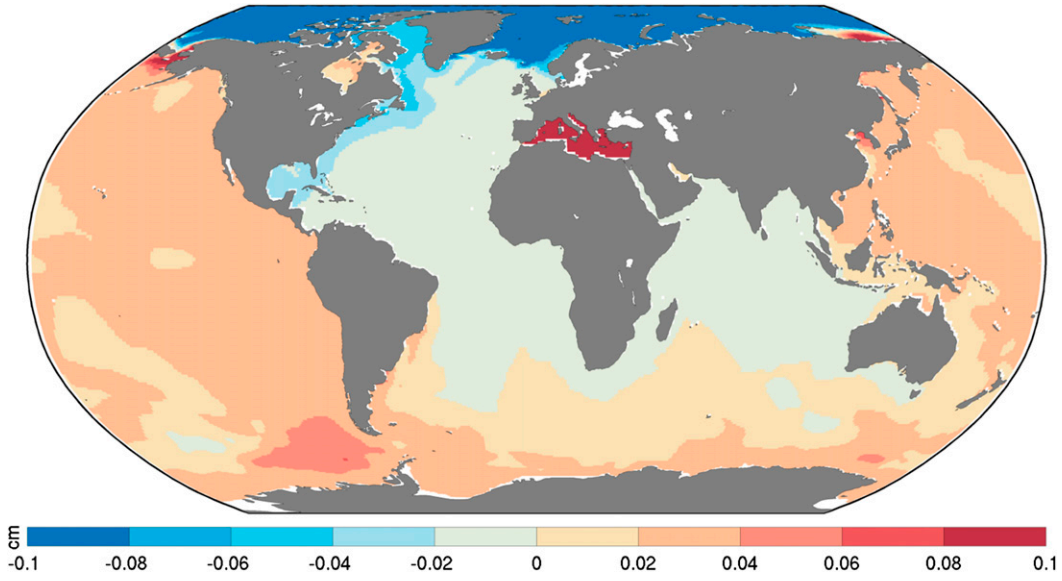

FIG. 8. First EOF mode of ξ_{DYN} explaining 42% of the total variance and computed using hourly output over a 1-month period.

adjustment of the mass field may not occur fast enough (e.g., Ponte 1993), other factors that can lead to deviations from equilibrium are related to coastal geometry and ocean depth. For example, the potential for nonequilibrium response increases where resonance can occur, such as in semienclosed regions like Hudson Bay associated with Helmholtz-type resonant response (e.g., Mullarney et al. 2008). Shallow bathymetry, as found for example in the coastal Arctic and Patagonian shelf, is another factor that can induce a stronger dynamic response (Fig. 7) because of factors such as a much slower gravity wave propagation and consequent longer adjustment time scales.

Apart from their primary high-frequency nature, ξ_{DYN} signals also tend to have relatively large spatial scales, which is generally expected because the larger the scales, the longer it should take to adjust the mass field. The large spatial scales of ξ_{DYN} are readily apparent from calculations of empirical orthogonal functions (EOF). From the example in Fig. 8, dynamic effects are dominated by large-scale, basinwide patterns with the same polarity in the Atlantic and Arctic and opposite polarity in the Pacific and Southern Ocean. Other features worth noting in Fig. 8 are the strong Arctic signals and the enhanced amplitude along the coast in the western Atlantic suggesting the involvement of boundary waves, possibly propagating from high latitudes.

5. Conclusions

Our main goals here were to include the full physics of SAL into an ocean model in a computationally efficient way and to assess the potential for dynamic behavior (i.e., departures from equilibrium) in the oceanic response to SAL effects as a function of location and time scale. In terms of computing cost, the implemented SAL package is very efficient and leads to an increase of the computation time by less than 6%, similar to (but smaller than) the values reported by Kuhlmann et al. (2011), who use similar method of Love number theory to compute SAL effects. The results confirm that implementation of SAL physics based on spherical harmonics becomes computationally feasible and is no longer prohibitive as found by Stepanov and Hughes (2004).

The effects of SAL associated with the variable ocean circulation, which we have examined, can result in measurable sea level signals, approaching 1 cm in places. Amplitudes of SAL-induced fluctuations are dependent on the size of the mass loads associated with the ocean circulation, and the omission of such effects amounts to approximately a 10% error in sea level values on average, which might be comparable to other model errors. Our results also indicate that simple parameterizations of SAL effects using constant scaling factors can induce further errors, in agreement with Stepanov and Hughes (2004).

An important innovation of this study and those of Stepanov and Hughes (2004) and Kuhlmann et al. (2011) is the ability to calculate potential dynamic signals associated with SAL effects. This dynamic response cannot be resolved, for example, by solving the sea level equation (Tamisiea et al. 2010), which is the more traditional approach. Our results show that the nature of the sea level

response to SAL strongly depends on location and time scale, with most energetic deviations from equilibrium occurring at time scales ranging from daily up to a week and reaching 1 cm in amplitude. The nonequilibrium response produced by SAL also tends to have a large-scale spatial structure. Shallow depths and constricted coastal geometries also seem to enhance the propensity for dynamic behavior. These features are very similar to those found in the oceanic response to other surface loads (Ponte 1993, 2006).

Given the presence of high-frequency dynamic fluctuations in sea level produced by the SAL effects and their importance compared to the total variability, studies dealing with changes in sea level on subweekly time scales might benefit from including SAL physics implicitly into ocean models. Examples include modeling of short-period tides (Ray 1998) and modeling of high-frequency signals to dealias satellite altimetry and gravity missions (Quinn and Ponte 2011). In studies of low-frequency variability, the dynamic component is not an issue as long as one is averaging sea level records over relatively long periods of time, that is, monthly and longer.

Finally, we recall that the only mass variations considered here are those produced by the variable ocean dynamics. In the future, it would be useful to examine the ocean response to SAL effects produced by other mass loadings such as high-frequency land hydrology and atmospheric pressure changes. One could also try joint simulations of the tides and the ocean circulation to examine how the full implementation of the physics of SAL used here can affect high-frequency tidal dynamics as well. These topics are left for future study.

Acknowledgments. This work was supported by the NASA Interdisciplinary Science Program through Grant NNX11AC14G and NSF Grant OCE-0961507, and partly by NASA Sea Level Change Team (N-SLCT) Project through Grant NNX14AP33G. We thank Gael Forget and Patrick Heimbach (MIT) for all their efforts on creating the model setup used in our experiments and for useful discussions on modeling issues.

REFERENCES

Accad, Y., and C. L. Pekeris, 1978: Solution of the tidal equations for the M2 and S2 tides in the world oceans from a knowledge of the tidal potential alone. *Philos. Trans. Roy. Soc.,* **A290,** 235–266, doi:10.1098/rsta.1978.0083.

Adcroft, A., C. Hill, J.-M. Campin, J. Marshall, and P. Heimbach, 2004: Overview of the formulation and numerics of the MITgcm. *Proc. ECMWF Seminar Series on Numerical Methods: Recent Developments in Numerical Methods for Atmosphere and Ocean Modelling,* Reading, United Kingdom, ECMWF, 139–149.

Arbic, B., S. T. Garner, R. W. Hallberg, and C. L. Simmons, 2004: The accuracy of surface elevations in forward global barotropic and baroclinic tide models. *Deep-Sea Res. II,* **51,** 3069–3101, doi:10.1016/j.dsr2.2004.09.014.

Blais, J. A. R., and D. A. Provins, 2002: Spherical harmonic analysis and synthesis for global multiresolution applications. *J. Geod.,* **76,** 29–35, doi:10.1007/s001900100217.

Campin, J.-M., A. Adcroft, C. Hill, and J. Marshall, 2004: Conservation of properties in a free surface model. *Ocean Modell.,* **6,** 221–244, doi:10.1016/S1463-5003(03)00009-X.

——, J. Marshall, and D. Ferreira, 2008: Sea ice–ocean coupling using a rescaled vertical coordinate z*. *Ocean Modell.,* **24,** 1–14, doi:10.1016/j.ocemod.2008.05.005.

Church, J. A., J. M. Gregory, N. J. White, S. M. Platten, and J. X. Mitrovica, 2011: Understanding and projecting sea level change. *Oceanography,* **24,** 130–143, doi:10.5670/oceanog.2011.33.

Dee, D. P., and Coauthors, 2011: The ERA-Interim reanalysis: Configuration and performance of the data assimilation system. *Quart. J. Roy. Meteor. Soc.,* **137,** 553–597, doi:10.1002/qj.828.

Driscoll, J. R., and D. Healy, 1994: Computing Fourier transforms and convolutions on the 2-sphere. *Adv. Appl. Math.,* **15,** 202–250, doi:10.1006/aama.1994.1008.

Farrell, W., and J. Clark, 1976: On postglacial sea level. *Geophys. J. Int.,* **46,** 647–667, doi:10.1111/j.1365-246X.1976.tb01252.x.

Gent, P. R., and J. C. McWilliams, 1990: Isopycnal mixing in ocean circulation models. *J. Phys. Oceanogr.,* **20,** 150–155, doi:10.1175/1520-0485(1990)020<0150:IMIOCM>2.0.CO;2.

Heimbach, P., D. Menemenlis, M. Losch, J. Campin, and C. Hill, 2010: On the formulation of sea-ice models. Part 2: Lessons from multi-year adjoint sea ice export sensitivities through the Canadian Arctic Archipelago. *Ocean Modell.,* **33,** 145–158, doi:10.1016/j.ocemod.2010.02.002.

Kopp, R. E., J. X. Mitrovica, S. M. Griffies, J. Yin, C. C. Hay, and R. J. Stouffer, 2010: The impact of Greenland melt on local sea levels: A partially coupled analysis of dynamic and static equilibrium effects in idealized water-hosing experiments. *Climatic Change,* **103,** 619–625, doi:10.1007/s10584-010-9935-1.

Kuhlmann, J., H. Dobslaw, and M. Thomas, 2011: Improved modeling of sea level patterns by incorporating self-attraction and loading. *J. Geophys. Res.,* **116,** C11036, doi:10.1029/2011JC007399.

Landerer, F. W., J. H. Jungclaus, and J. Marotzke, 2007: Regional dynamic and steric sea level change in response to the IPCC-A1B scenario. *J. Phys. Oceanogr.,* **37,** 296–312, doi:10.1175/JPO3013.1.

Large, W. G., J. C. McWilliams, and S. C. Doney, 1994: Ocean vertical mixing: A review and a model with a nonlocal boundary layer parameterization. *Rev. Geophys.,* **32,** 363–403, doi:10.1029/94RG01872.

Losch, M., D. Menemenlis, J. M. Campin, P. Heimbach, and C. Hill, 2010: On the formulation of sea-ice models. Part 1: Effects of different solver implementations and parameterizations. *Ocean Modell.,* **33,** 129–144, doi:10.1016/j.ocemod.2009.12.008.

Marshall, J. C., C. Hill, L. Perelman, and A. Adcroft, 1997: Hydrostatic, quasi-hydrostatic, and non-hydrostatic ocean modeling. *J. Geophys. Res.,* **102,** 5733–5752, doi:10.1029/96JC02776.

Milne, G. A., W. R. Gehrels, C. W. Hughes, and M. E. Tamisiea, 2009: Identifying the causes of sea-level change. *Nat. Geosci.,* **2,** 471–478, doi:10.1038/ngeo544.

Mitrovica, J. X., M. E. Tamisiea, J. L. Davis, and G. A. Milne, 2001: Recent mass balance of polar ice sheets inferred from patterns of global sea-level change. *Nature,* **409,** 1026–1029, doi:10.1038/35059054.

Mullarney, J. C., A. E. Hay, and A. J. Bowen, 2008: Resonant modulation of the flow in a tidal channel. *J. Geophys. Res.,* **113,** C10007, doi:10.1029/2007JC004522.

Ponte, R. M., 1993: Variability in a homogeneous global ocean forced by barometric pressure. *Dyn. Atmos. Oceans,* **18,** 209–234, doi:10.1016/0377-0265(93)90010-5.

——, 1999: A preliminary model study of the large-scale seasonal cycle in bottom pressure over the global ocean. *J. Geophys. Res.,* **104,** 1289–1300, doi:10.1029/1998JC900028.

——, 2006: Oceanic response to surface loading effects neglected in volume-conserving models. *J. Phys. Oceanogr.,* **36,** 426–434, doi:10.1175/JPO2843.1.

——, and S. V. Vinogradov, 2007: Effects of stratification on the large-scale ocean response to barometric pressure. *J. Phys. Oceanogr.,* **37,** 245–258, doi:10.1175/JPO3010.1.

Quinn, K. J., and R. M. Ponte, 2011: Estimating high frequency ocean bottom pressure variability. *Geophys. Res. Lett.,* **38,** L08611, doi:10.1029/2010GL046537.

——, and ——, 2012: High frequency barotropic ocean variability observed by GRACE and satellite altimetry. *Geophys. Res. Lett.,* **39,** L07603, doi:10.1029/2012GL051301.

Ray, R. D., 1998: Ocean self-attraction and loading in numerical tidal models. *Mar. Geod.*, **21,** 181–192, doi:10.1080/01490419809388134.

Redi, M. H., 1982: Oceanic isopycnal mixing by coordinate rotation. *J. Phys. Oceanogr.,* **12,** 1154–1158, doi:10.1175/1520-0485(1982)012<1154:OIMBCR>2.0.CO;2.

Riva, R. E. M., J. L. Bamber, D. A. Lavalleé, and B. Wouters, 2010: Sea-level fingerprint of continental water and ice mass change from GRACE. *Geophys. Res. Lett.,* **37,** L19605, doi:10.1029/2010GL044770.

Speer, K., and G. Forget, 2013: Global distribution and formation of mode waters. *Ocean Circulation and Climate: A 21st Century Perspective,* G. Siedler et al., Eds., Elsevier, 211–226.

Stammer, D., A. Cazenave, R. M. Ponte, and M. E. Tamisiea, 2013: Causes for contemporary regional sea level changes. *Annu. Rev. Mar. Sci.,* **5,** 21–46, doi:10.1146/annurev-marine-121211-172406.

Stepanov, V. N., and C. W. Hughes, 2004: Parameterization of ocean self-attraction and loading in numerical models of the ocean circulation. *J. Geophys. Res.,* **109,** C07004, doi:10.1029/2003JC002034.

Stocker, T. F., and Coauthors, Eds., 2014: *Climate Change 2013: The Physical Science Basis.* Cambridge University Press, 1535 pp.

Tamisiea, M. E., E. Hill, R. M. Ponte, J. L. Davis, I. Velicogna, and N. T. Vinogradova, 2010: Impact of self-attraction and loading on the annual cycle in sea level. *J. Geophys. Res.,* **115,** C07004, doi:10.1029/2009JC005687.

Vinogradova, N. T., R. M. Ponte, and D. Stammer, 2007: Relation between sea level and bottom pressure and the vertical dependence of oceanic variability. *Geophys. Res. Lett.,* **34,** L03608, doi:10.1029/2006GL028588.

——, ——, M. E. Tamisiea, J. L. Davis, and E. M. Hill, 2010: Effects of self-attraction and loading on annual variation of ocean bottom pressure. *J. Geophys. Res.,* **115,** C06025, doi:10.1029/2009JC005783.

——, ——, ——, K. J. Quinn, E. M. Hill, and J. L. Davis, 2011: Self-attraction and loading effects on ocean mass redistribution at monthly and longer time scales. *J. Geophys. Res.,* **116,** C08041, doi:10.1029/2011JC007037.

Wunsch, C., and P. Heimbach, 2013: Dynamically and kinematically consistent global ocean circulation and ice state estimates. *Ocean Circulation and Climate: A 21st Century Perspective,* G. Siedler et al., Eds., Elsevier, 553–580.

Yin, J., S. M. Griffies, and R. J. Stouffer, 2010: Spatial variability of sea-level rise in the 21st century projections. *J. Climate,* **23,** 4585–4607, doi:10.1175/2010JCLI3533.1.